# Characterization of spin-state tuning in thermally annealed semiconductor quantum dots

E. Margapoti,[1] Fabrizio M. Alves,[2] S. Mahapatra,[3] T. Schmidt,[1] V. Lopez-Richard,[2] C. Destefani,[2] E. Menéndez-Proupin,[4] Fanyao Qu,[5] C. Bougerol,[6] K. Brunner,[3] A. Forchel,[1] G. E. Marques,[2] and L. Worschech[1]

[1]*Technische Physik, Physikalisches Institut, Universität Würzburg, Am Hubland, 97074 Würzburg, Germany*
[2]*Departamento de Física, Universidade Federal de São Carlos, 13560-905 São Carlos, SP, Brazil*
[3]*Experimentelle Physik III, Physikalisches Institut, Universität Würzburg, Am Hubland, 97074 Würzburg, Germany*
[4]*Departamento de Física, Facultad de Ciencias, Universidad de Chile, Las Palmeras 3425, 780-0024 Ñuñoa, Santiago, Chile*
[5]*Instituto de Física, Universidade de Brasília, 608400-902 Brasília, DF, Brazil*
[6]*SP2M/DRFMC/CEA-Grenoble, CEA-CNRS NPSC, 17 rue des Martyrs, 38054 Grenoble Cedex, France*

We report a systematic study of magneto-optical properties in CdZnSe/ZnSe semiconductor quantum dots (QDs) subjected to postgrowth thermal annealing. The theoretical and experimental characterizations are combined in order to understand the evolution of Zeeman splitting and the blueshift as well as redshift of the magnetic subcomponents with magnetic field strength of excitons confined in annealed QDs as a function of different annealing times. A combination of a multiband model as well as parameter interpolation supported by *ab initio* calculations is presented and points toward an inversion of the light-hole-heavy-hole states due to annealing. The band mixing of exciton states explains besides the variation in the Zeeman splitting for differently annealed QD excitons, the evolution of the diamagnetic blueshift into a paramagnetic redshift of the magnetic subcomponents. A discussion of the effects associated to the Coulomb interaction on the polarized excitonic recombinations modulated by magnetic field is given.

## I. INTRODUCTION

The growth of multicompound semiconductor quantum dots (QDs) can offer a much broader range of possible structural modifications than those obtained from single-component semiconductors since tunable characteristics that depend on composition and shape of confinement region can be exploited.[1–4] In addition to the size and composition effects, thermal annealing (TA) principally also allows the control of the lattice structure for compound semiconductor QDs due to vast changes in the compound composition.[5] As a consequence, one may expect distinct changes in the electronic as well as magnetic properties of QD confined carriers caused by thermal annealing. Though, thermally annealed QDs have been studied motivated by structural enhancements, e.g., better QD homogeneity, tuning of emission wavelengths,[6–10] and improving quantum efficiency,[11–14] the role of thermal annealing on magnetic properties of II-VI QDs has been studied just recently.[15–17]

It is the purpose of this work to develop a characterization of QD electronic structure that would enable the analysis of magnetic field effects, shape, composition, and interband coupling within the same framework. These results are compared and tested with experiments in order to understand several general trends observed in the optical response of thermally annealed CdZnSe/ZnSe QDs under an applied magnetic field. The search for peculiar nuances in the optical response of single-QD systems is on the focus of recent and experimental endeavors[18–21] to which this paper may contribute with its findings and discussion.

Thermal annealing effects on the electronic properties of semiconductor nanostructures have been studied for some time. These processes can be characterized by analyzing its influence on the dynamics of system composition and geometry[9,22–24] that can be simulated theoretically. The study of the electronic and magnetic properties of semiconductor QDs has been the focus of recent theoretical endeavors[25–31] that have systematically complemented the experimental findings.

In this work, we discuss the role of an externally applied magnetic field on the electronic structure of thermally annealed QDs by consideration of size, shape, as well as variations in chemical composition. We compare our theoretical analysis with magneto-optical studies conducted with annealed CdZnSe/ZnSe QDs. In particular, the circularly polarized photoluminescence (PL) of QDs subject to magnetic fields was studied. The theory captures the experimentally observed modulation of the Zeeman splitting as well as diamagnetic and paramagnetic shifts due to thermal annealing. Several key factors that can be used for the manipulation of spin states are revealed.

## II. EXPERIMENTAL RESULTS

The experimental measurements reported in this work were carried out on CdZnSe/ZnSe QDs. Two samples were analyzed, grown by molecular-beam epitaxy: (i) with 2 monolayers (MLs) of CdSe and (ii) with 3 MLs CdSe. After the sample growth, rapid thermal annealing was performed with an annealing temperature of 500 °C and different annealing times ranging from 10 to 80 s. Details can be found in Ref. 17. TA leads to a blueshift of the QD emission. In addition a narrowing of the inhomogeneously broadened QD emission takes place, which was interpreted in terms of TA-induced interdiffusion of atoms, in particular, a decrease in the Cd content and an increase in Zn content in the QDs takes place, which in turn leads to several changes in QD parameters.
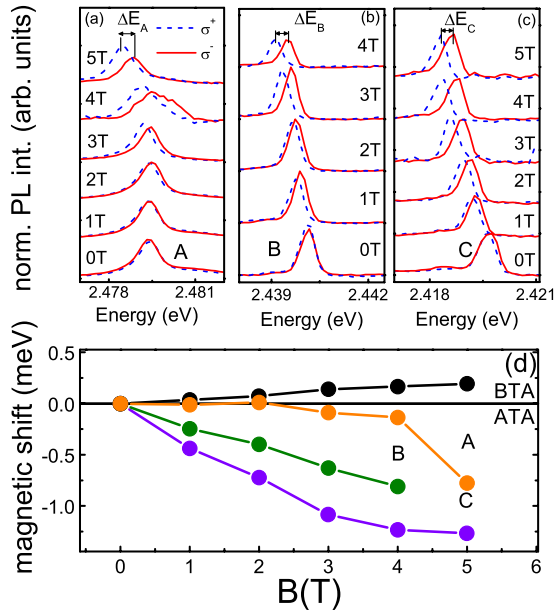
FIG. 1. (Color online) Magnetic response of single QD excitons confined in annealed QDs. (a) $\sigma^+$ and $\sigma^-$ circularly polarized component of a single QD A after TA, recorded from 0 to 5 T. (b) $\sigma^+$ and $\sigma^-$ circularly polarized component of a single QD B after TA, recorded from 0 to 4 T. (c) $\sigma^+$ and $\sigma^-$ circularly polarized component of a single QD C after TA, recorded from 0 to 5 T. (d) Magnetic shift for the single QD emissions before and after TA for both *dotA* and *dotB*.

After thermal annealing (ATA), the samples were excited by an argon ion laser and the QD PL was studied in a cryostat equipped with magnetic coils. The sample temperature was 2–5 K. By means of polarizers the circular polarized QD emission was studied for different magnetic field strengths. The PL emission was then analyzed with respect to the peak splitting and the peak shift. Typically, QD excitons show a blueshift of the center of gravity of the magnetic subcomponents when the magnetic field strength is raised, which is often referred to as diamagnetic shift. In this study also a redshift of the center of gravity of the Zeeman subcomponents was observed for annealed QDs. It is argued that due to TA the light-hole (lh) bands can substantially mix with the exciton ground state. It is the aim of the analysis here to present the evolution of the Zeeman splitting and, in particular, of the magnetic shift of the magnetic subcomponents when thermal annealing was performed.

In Fig. 1, the right and left circularly polarized ($\sigma^\pm$) PL spectra for three different single QDs, nominally *dotA*, *dotB*, and *dotC*, recorded at different magnetic fields, are shown. Figure 1(a) shows the spectra for the *dotA*, which was recorded up to 5 T, in Fig. 1(b) are shown the spectra of *dotB* recorded up to 4 T and finally, in Fig. 1(c) the *dot C* spectra recorded up to 5 T are shown. We should mention that these three QDs were recorded from different samples.

With increasing $B$ the Zeeman splitting, $\Delta E_{(A,B,C)}$, increases. It is interesting to note that both $\sigma^+$ and $\sigma^-$ polarized peaks of the QD emission show a red shift that increases with the magnetic field strength. For a better analysis, the center of gravity of the two Zeeman components of each QD,
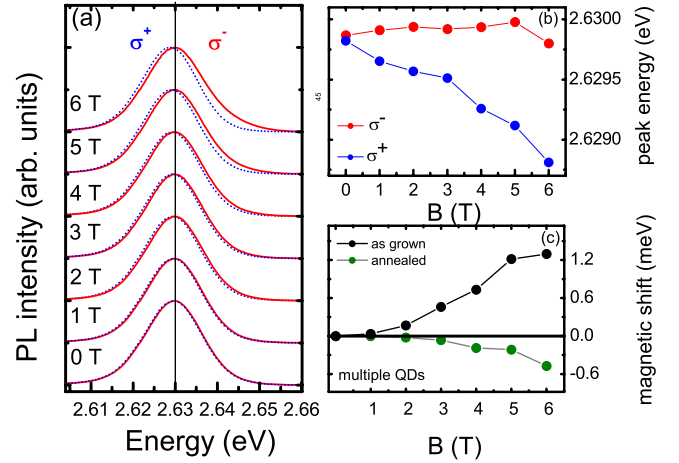


FIG. 2. (Color online) Magnetic response of multiple QD excitons confined in annealed QDs. (a) Multiple QD spectra after annealing at various magnetic fields. (b) Peak positions of polarized components for the multiple QD emission. (c) Magnetic shift for the multiple QD emission before and after annealing.

$\bar{E}(B) = [E_{\sigma^+}(B) + E_{\sigma^+}(B)]/2 - E(0)$ (further referred to as magnetic shift), is presented in Fig. 1(d). Such a behavior is also corroborated in the emission of an ensemble of QDs as displayed in Figs. 2(a)–2(c), respectively. The value of $\bar{E}(B)$ for as-grown QDs, both for single-dot PL line (spectra not shown) as for multiple dot emissions, shows the expected weak diamagnetic blueshift, with increasing $B$. For thermally annealed QDs, the magnetic shift is indeed negative and about −0.78 meV for $B = 5$ T in the case of *dotA*, −0.8 meV for $B = 4$ T in case of *dotB* and −1.26 meV in case of *dotC*. Also, in Fig. 1(d), the magnetic shift of the three QDs is shown. We should point out that the three QDs show a different trend. Indeed, while *dotA* shows a slow increase in the magnetic shift with $B$ up to 4 T, *dotB* shows a linear increase. Whereas, *dotC* increases linearly, as *dotB* does up to $B = 4$ T, but saturates between $B = 4–5$ T. Therefore, the TA process leads to an anomalous sign inversion of the effective magnetic shift while the amplitude of the shift changes from dot to dot.

To model our observations we have considered the modulation of the electronic structure due to TA including an increase in the bulk band-gap energy. This was done in our model by taking into account the parameters reported for $Cd_xZn_{1-x}Se$ with $x$ the Cd content, using Ref. 32. Besides the Cd-content reduction, also a decrease in the confinement strength takes place. The QD excitonic corrections for the binding energy should also be analyzed in terms of the structure parameters to assess its relative effect on the optical recombination energy. Finally, high resolution transmission electron microscopy (HRTEM) images for different QDs have shown that the average dot size increases during the thermal annealing process.[17]

In order to shed light on the exciton nature that shows a paramagnetic shift, a variation of the excitation power of a single QD was performed. The signature of different excitonic complexes was then analyzed. In Fig. 3(a), the magnetic-field-induced redshift of a single-dot emission (af-
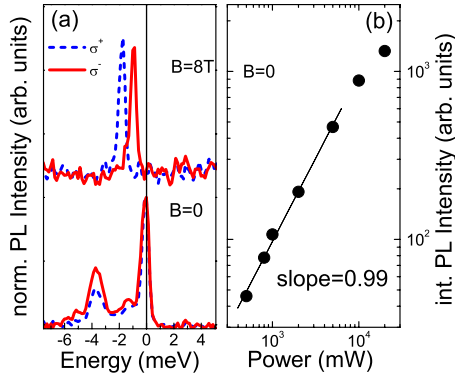
FIG. 3. (Color online) (a) PL spectra of a single QD after TA at **B**=0 and **B**=8 T and (b) PL intensity dependence on excitation power at **B**=0.



FIG. 5. (a) and (b) measured Zeeman splitting and magnetic shift, respectively, at **B**=6 T as the annealing time increases for samples with different sizes.

ter annealing) is displayed. The intensity values of the corresponding power series of this emission (at $B=0$) are shown in Fig. 3(b). The slope of this curve strengthens the hypothesis of a recombination from a neutral exciton.[33] In Fig. 4 the magnetic shift recorded at 7 T for several differently annealed QDs is shown, where, except for QD4, all other measured peaks of QD emission are redshifted after TA due to the application of a magnetic field.

The spin splitting tuning with annealing time is represented in Fig. 5(a) for samples with 2 and 3 ML at **B**=6 T. The $g$ factors of QDS determined prior to thermal annealing vary significantly. As the annealing evolves, the QDs show a minimum Zeeman splitting at annealing $t_a=20-30$ s. Moreover, the $g$ factor for the sample grown with the 2 MLs CdSe changes sign due to annealing. Above $t_a=50$ s all three samples show a comparable small and constant Zeeman splitting. Also, according to Fig. 5(b), the magnetic shift suffers a continuous variation and changes sign. In particular, it becomes negative.

### III. THEORETICAL MODEL

In order to understand the dynamics of the Zeeman splitting and the magnetic shift involved in the thermal annealing processes and its effect on the electronic structure we have performed a multiband calculation. For mathematical simplification but without any loss of generality we model a single $Cd_xZn_{1-x}Se$ QD by a cylindrical spatial confinement region



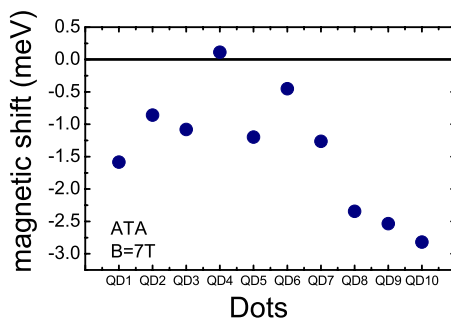FIG. 4. (Color online) Trend of the magnetic shift for several single QDs after TA at the magnetic field of **B**=7 T.
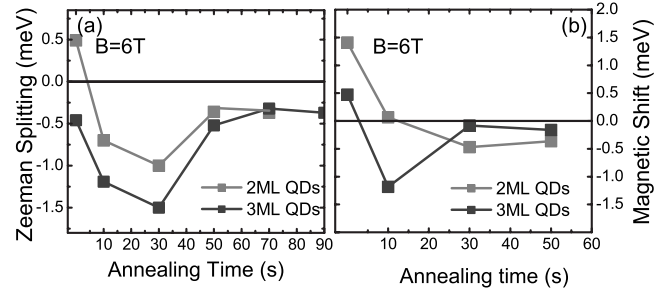
of radius $R$ and height $L_z$. The band parameters for the compound material have been taken as a function of the Cd-content $x$.[32] If no reference is found for a given band parameter at intermediary values of $x$, a linear interpolation between the corresponding reported values for ZnSe ($x=0$) and CdSe ($x=1$) was applied, based on the virtual crystal approximation approach. This model can characterize properly the QD shape and magnetic field effects within the same framework by including the most important aspects of valence-band admixture effects that are at the root of several experimental observations. Given that strain parameters are of critical importance we performed an estimation of the Cd-content dependence for the elastic constants by using an *ab initio* approach in order to validate the use of linear interpolations.

The single-particle Hamiltonian for the QD has been approached by using a parabolic axial confinement emulating a smooth transition for any composition fluctuation from the central area of the dot to the bordering substrate. The axial $[\rho^2=(x^2+y^2)]$ and longitudinal ($z$) coordinates inside this cylindrically shaped QDs can be treated as separable variables, without any loss of generality, even in the presence of a magnetic field applied along the longitudinal direction.

### A. Conduction band

For this cylindrical confinement, the conduction-band Hamiltonian for an electron with effective mass $m^* \times m_0$ inside a QD as confined to a parabolic potential can be given

$$\mathcal{H} = \mathcal{H}_{xy} + \frac{\hbar^2}{2m^*m_0}\hat{k}_z^2 + V(z), \tag{1}$$

where $V(z)$ is the confinement potential along the longitudinal or growth direction, $z$, and the lateral Hamiltonian is a bidimensional harmonic oscillator problem with number operators, $\hat{N}_{\pm}=a_{\pm}^{\dagger}a_{\pm}$ given in terms of creation and annihilation operators, $a_{\pm}^{\dagger}$ and $a_{\pm}$, as

$$\mathcal{H}_{xy} = \frac{\hbar}{m^*}\omega_0(\hat{N}_+ + \hat{N}_- + 1). \tag{2}$$

Here, $\omega_0=\hbar/m_0R^2$ is an axial parabolic frequency.

The eigenstates of Eq. (2) can be labeled by quantum numbers $n_+,n_-=0,1,2,\ldots$ where the eigenstates $|n_+,n_-\rangle$ obey the eigenvalue equations, $\hat{N}_{\pm}|n_+,n_-\rangle=n_{\pm}|n_+,n_-\rangle$. The

corresponding normalized eigenfunctions are given by

$$\Psi_{n_+,n_-}(\rho,\phi) = \langle\rho,\phi|n_+,n_-\rangle = \frac{1}{\sqrt{2\pi}} F_{n_+,n_-}(\rho)\exp[i(n_+ - n_-)\phi],$$

(3)

$$F_{n_+,n_-}(\rho) = \frac{\sqrt{2}}{R}\sqrt{\frac{\alpha_{n_+,n_-}!}{(\alpha_{n_+,n_-} + |n_+ - n_-|)!}}\left(\frac{\rho}{R}\right)^{|n_+-n_-|}$$

$$\times\exp\left(-\frac{\rho^2}{2R^2}\right)L_{\alpha_{n_+,n_-}}^{|n_+-n_-|}\left(\frac{\rho^2}{R^2}\right),$$

(4)

where $\alpha_{n_+,n_-} = \min(n_+,n_-)$ and $L_p^q(x)$ is the associated Laguerre polynomial function defined for a pair of positive integer numbers $p$, $q$. According to Eq. (2), the states $|n_+,n_-\rangle$, such that $(n_+ + n_-) = \text{const}$ remain degenerate and this description is valid only in the absence of a magnetic field. The application of a magnetic field to the QD lifts this degeneracy.

When a uniform magnetic field, $\mathbf{B} = B\hat{\mathbf{z}}$ is applied along the symmetry axis, $z$, it affects the electronic states in the perpendicular plane giving rise to the quantization of the angular momentum, $\hat{\ell}_z = (\hat{N}_+ - \hat{N}_-)$, with eigenvalues $m = (n_+ - n_-) = 0, \pm 1, \pm 2, \ldots$ Thus, an effective renormalization is introduced to the axial quantization, $V_B = m_0/m^*\omega_c^2\rho^2/8$, where $\omega_c = eB/m_0c$ is the cyclotron frequency. The momentum operators, perpendicular to the field transform to

$$\hat{k}_\pm = i(c_\pm a_\pm^\dagger - c_\mp a_\mp),$$

(5)

where $c_\pm^2 = \frac{m_0}{\hbar}(\frac{\omega_c^2}{\Omega} + \Omega \pm \omega_c)$, and the new Hamiltonian for the lateral motion is given by

$$\mathcal{H}_{xy} = \frac{1}{m^*}\left[\hbar\omega_+\left(\hat{N}_+ + \frac{1}{2}\right) + \hbar\omega_-\left(\hat{N}_- + \frac{1}{2}\right)\right] + \frac{g_0\mu_B}{2}B\sigma_z,$$

(6)

where $\Omega = \sqrt{\omega_0^2 + \omega_c^2/4}$ is a frequency associated with the competition between spatial and magnetic confinements, $\omega_\pm = \Omega \pm \omega_c/2$, $\mu_B = e\hbar/2m_0c$ is the Bohr magneton, $g$ is the electron Landé factor, and $\sigma_z$ is the $z$-component Pauli matrix. The corresponding eigenvalues of Hamiltonian (6) are

$$E_{n_+,n_-,\sigma_z} = \frac{1}{m^*}\left[\hbar\Omega(n_+ + n_- + 1) + \frac{1}{2}\hbar\omega_c(n_+ - n_-)\right] + g_0\mu_B B\frac{\sigma_z}{2}$$

(7)

and the eigenfunctions are obtained from Eq. (4), after replacing $R$ by $\ell = \sqrt{\hbar/m_0\Omega}$. In the strong magnetic field regime, when $R \gg \sqrt{\hbar/m_0\omega_c}$, the usual Landau-level quantization is recovered,

$$E_{n_+} \simeq \frac{\hbar\omega_c}{m^*}\left(n_+ + \frac{1}{2}\right) \pm \frac{1}{2}g_0\mu_B B.$$

(8)

Only in the limiting case, $\omega_c \gg \omega_0$, the effects of the lateral confinement can be neglected. As mentioned before the lateral and longitudinal confinements can be treated separately and we use an infinite wall model in the Hamiltonian

$$\mathcal{H}_z = -\frac{1}{m^*}\left(\frac{\hbar^2}{2m_0}\hat{k}_z^2\right) + V(z)$$

(9)

that have eigenvalues,

$$E_\nu = \frac{1}{m^*}\left(\frac{\hbar^2\pi^2\nu^2}{2m_0L_z^2}\right) \quad (\nu = 1,2,3,\ldots).$$

(10)

As seen, we have chosen to indicate the material parameters in terms of the bare electron mass $m_0$, instead of the effective mass, in order to keep a coherence between the labels used for electrons as similar as for holes.

### B. Valence band

The description of electronic states in the valence band must go beyond the parabolic band approximation, a crucial requirement when describing interband optical transitions between confined states. Several aspects of the optical properties in quantum dots can be found in Refs. 25–31.

The use of an $8 \times 8$ models in Refs. 25–29 has been justified by the relatively narrow gap in the CdTe structures. However, in the majority of the situations describing wide-gap semiconductor states in nanostructures, the multiband Luttinger Hamiltonian model is a fairly good approximation (in ZnSe $E_g > 2$ eV). The right choice for the basis set requires deep analysis and exploration of symmetries in each case. The eigenfunctions of Eq. (6) can be searched by using the commutation and anticommutation relations between momentum operator components, $\hat{k}_\pm = (\hat{k}_x \pm \hat{k}_x)$, in the form

$$\{\hat{k}_+,\hat{k}_-\} = \left(\hat{N}_+ + \frac{1}{2}\right)c_+^2 + \left(\hat{N}_- + \frac{1}{2}\right)c_-^2 - c_+c_-(a_+^\dagger a_-^\dagger + a_+a_-),$$

(11)

$$[\hat{k}_+,\hat{k}_-] = -c_+^2 + c_-^2.$$

(12)

Using the definition of Eq. (5), the Luttinger Hamiltonian assumes the form

$$\mathcal{H}_L = \begin{bmatrix} D_{hh}^{(+)} & A_- & 0 & B \\ & D_{lh}^{(+)} & B & 0 \\ & & D_{hh}^{(-)} & A_+ \\ & & & D_{lh}^{(-)} \end{bmatrix},$$

(13)

where the diagonal matrix operators are given by

$$D_{hh}^{(\pm)} = -\left(\frac{\bar{\gamma}_1 + \bar{\gamma}_2}{2}\right)\{\hat{k}_+,\hat{k}_-\} - \left(\frac{\bar{\gamma}_1 - 2\bar{\gamma}_2}{2}\right)\hat{k}_z^2 \pm \frac{3}{4}\left(\bar{\kappa} + \frac{9}{4}\bar{q}\right)$$

$$\times[\hat{k}_+,\hat{k}_-] + \delta E_{hh}$$

(14)

and

$$D_{lh}^{(\pm)} = -\left(\frac{\bar{\gamma}_1 - \bar{\gamma}_2}{2}\right)\{\hat{k}_+,\hat{k}_-\} - \left(\frac{\bar{\gamma}_1 + 2\bar{\gamma}_2}{2}\right)\hat{k}_z^2 \pm \frac{1}{4}\left(\bar{\kappa} + \frac{1}{4}\bar{q}\right)$$

$$\times[\hat{k}_+,\hat{k}_-] + \delta E_{lh}.$$

(15)

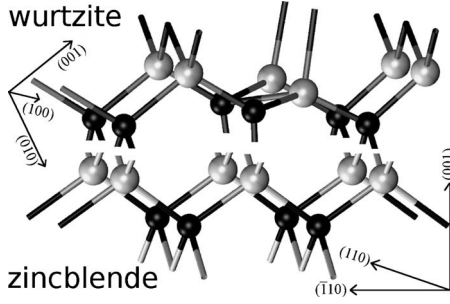The indexes hh or lh, in Eqs. (14) and (15), label the heavy-

FIG. 6. Illustration of (001) surface of zinc blende with the matching wurtzite surface of CdSe-ZnSe. Created with the GDIS (Ref. 34), VMD (Ref. 35), and GIMP (Ref. 36).

and light-hole carriers, respectively. The off-diagonal matrix operators are defined as, $A_{\pm} = \mp \sqrt{3} \bar{\gamma}_3 \hat{k}_{\pm} \hat{k}_z$ and $B = -\frac{\sqrt{3}}{2} \bar{\gamma} \hat{k}_{-}^2$, where $\bar{\gamma}_i = \frac{\hbar^2}{m_0} \gamma_i$ $(i = 1, 2, 3)$ and $\bar{\kappa} = \frac{\hbar^2}{m_0} \kappa$, $\bar{q} = \frac{\hbar^2}{m_0} q$, and $\bar{\gamma} = (\bar{\gamma}_2 + \bar{\gamma}_3)/2$ are the Luttinger effective mass and magnetic parameters defining the inherent admixture between hole spin states.

Hamiltonian (13), after replacing $R$ by $\ell = \sqrt{\hbar/m_0 \Omega}$, is expanded in the infinite basis set of functions [Eq. (3)]. A convergency truncation is chosen such that the addition of a new function would not induce any significant change on the energies of the first few excited eigenstates of any carrier. Using this model and the usual computational procedures we have performed a systematic analysis of the annealing time dependence of QD properties associated to size and composition, taken with function $x(t_a)$ of Eq. (1).

## IV. STRAIN EFFECTS AND *AB INITIO* PARAMETERS

Although bulk CdSe is known to have a predominant stable wurtzite structure, the growth of narrow layer CdZnSe QDs with predominant wurtzite phase over a (001) zinc-blende buffer layer is rather unlikely. Whereas the (001) zinc-blende surface has a twofold rotation axis, the wurtzite structure only has a threefold rotation axis, along with twofold and sixfold screw axes that are incompatible with surfaces. We have explored the possibility to match a wurtzite structure over a (001) zinc-blende surface, keeping the maximum number of tetrahedral bonds. As shown in Fig. 6, matching wurtzite and zinc-blende surfaces requires duplication of bonds or vacancies at some sites, causing very high surface energy. Moreover, the wurtzite lattice would be strained in order to match the substrate lattice vectors in the directions $(\bar{1}10)$ and $(110)$. Hence, we assume that the quantum dot has zinc-blende structure.

Due to the large mismatch between the zinc-blende CdSe and ZnSe lattice parameters, the strain correction effects must be considered in the few monolayer CdZnSe dot structure. These corrections affect directly the energy band gap (hydrostatic contribution) and lifts (axial contribution) the degeneracy of heavy and light holes at the center of Brillouin zone. We assume a uniform strain distributions for the heavy- and light-hole energy corrections given by[37]

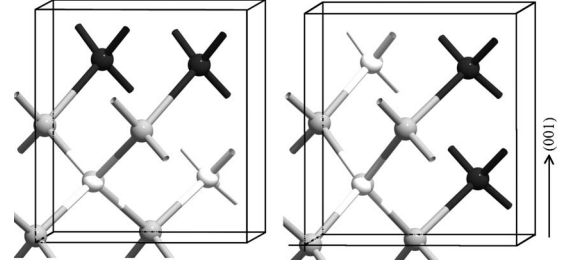$$\delta E_{hh}(x) = \epsilon_h(x) + \epsilon_s(x) \qquad (16)$$

and



FIG. 7. Structural models for $Cd_{0.5}Zn_{0.5}Se$. Left panel: the model 1 has similar atoms (Cd or Zn) in the same layer. Right panel: the model 2 displays similar atoms in different layers. Color scheme: Zn: white, Cd: black, and Se: gray. Created with GDIS (Ref. 34) and GIMP (Ref. 36).

$$\delta E_{lh}(x) = \epsilon_h(x) - \epsilon_s(x) - 2 \frac{\epsilon_s^2(x)}{\Delta(x)}. \qquad (17)$$

Here, $\Delta(x)$ is the spin-orbit splitoff, $\epsilon_h$ and $\epsilon_s$ are the hydrostatic and the shear strain contributions to the effective energy gap. They can be written in terms of deformation potentials $a_v$, $b$ and the elastic constants $C_{ij}$ as[38]

$$\epsilon_h(x) = 2a_v(x) \frac{C_{11}(x) - C_{12}(x)}{C_{11}(x)} \epsilon(x) \qquad (18)$$

and

$$\epsilon_s(x) = -b(x) \frac{C_{11}(x) + 2C_{12}(x)}{C_{11}(x)} \epsilon(x), \qquad (19)$$

where $\epsilon(x) = [a_S - a_{dot}(x)]/a_{dot}(x)$ and $a_S$ is the lattice constant of the ZnSe substrate and $a_{dot}(x)$ is the lattice constant of unstrained $Cd_xZn_{1-x}Se$. This approximation is fair for the ground state of narrow QD since the strain distribution near the interfaces has a very small influence on its average value.[39]

In order to evaluate the Cd-content dependence of the lattice parameters and the elastic constants, we have performed an *ab initio* calculation within the local-density approximation (LDA),[40] as implemented within the Vienna *ab initio* simulation package (VASP).[41] The wave functions were expanded in plane waves with an energy cutoff of 320 eV. The $6 \times 6 \times 6$ Monkhorst-Pack grid of $k$ points was used to sample the reciprocal unit cell corresponding to the eight atoms cubic supercell shown in Fig. 7. With these settings we have obtained energies, pressures, and forces converged within 1 meV/atom, 1.1 kbar, and 1 meV/Å, respectively. Fitting the *ab initio* $P$-$V$ data with the Birch-Murnaghan equation,[42] we obtained the null pressure theoretical lattice constant $a_{ZnSe} = 5.5739$ Å, which is 1.7% smaller than the reported experimental value, 5.6676 Å. For CdSe we have obtained $a_{CdSe} = 6.0208$ Å, which is 0.9% smaller than the reported experimental value, 6.077 Å. These results can be considered in excellent agreement and, besides, they follow the general well-known trend of the LDA approximation to underestimate lattice constants.

Table I and Fig. 8 show the *ab initio* values of the $Cd_xZn_{1-x}Se$ lattice constant and in-plane stress tensor for the heterostructure. The in-plane stresses have been estimated

TABLE I. Calculated $Cd_xZn_{1-x}Se$ lattice constant and stress values for the QD structure.

| Material | $a$ | $\sigma_{xx}$ (GPa) |
|---|---|---|
| CdSe | 6.0208 | 4.2 |
| $Cd_{0.75}Zn_{0.25}Se$ | 5.9067 | 3.58 |
| $Cd_{0.5}Zn_{0.5}Se$ | 5.7947 | 2.54 |
| $Cd_{0.25}Zn_{0.75}Se$ | 5.6852 | 1.52 |
| ZnSe | 5.5739 | 0.0 |

using bulk calculations of model supercells of $Cd_xZn_{1-x}Se$, where the (100) and (010) lattice vectors were fixed to the ZnSe vectors while the atomic positions and cell dimension in the (001) direction were allowed to relax. The structural modeling for CdSe uses a cubic eight-atom supercell subjected to tetragonal deformation. The different ternary alloys have been crudely simulated using this same supercell after the replacement of one, two or three Cd by Zn atoms in each ternary alloy with Cd content: $x=0.75$, 0.5, and 0.25, respectively. In structures having Cd content with $x=0.25$ and 0.75, the positions of all minority atoms are equivalent. However, for $x=0.5$ it is possible to form two different structures which are shown in Fig. 7. In the first model, the Cd atoms are in one plane parallel to the growth plane whereas the Zn atoms are in the other plane. In model 2, each plane contains one Cd and one Zn atom. Due to these spatial symmetries, models 1 and 2 may have two and four equivalent growth configurations, respectively. Therefore, the stress tensor of the alloy can be obtained by averaging these two models (Table II) with the Boltzmann factor at the growth temperature, $T=573$ K.

The *ab initio* values of the stress tensor component, $\sigma_{xx}$, are consistent with a linear interpolation of the elastic constants as a function of the Cd content, $x$. Hence, it is safe to use a linear interpolation of the experimental elastic moduli $C_{11}$, $C_{12}$, and $C_{44}$ (Ref. 43) in our multiband calculation. Moreover, we assume that the deformation potentials can also be linearly interpolated between the reported values for CdSe and ZnSe, as taken from Ref. 44.
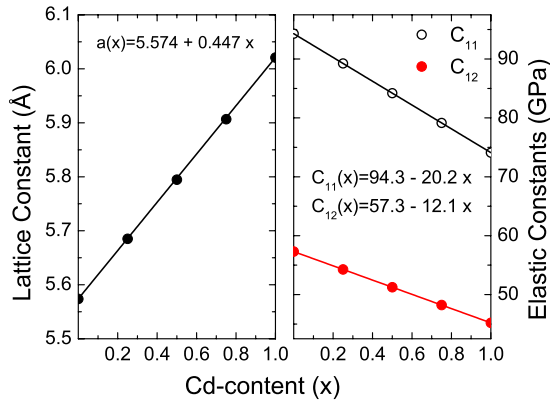


FIG. 8. (Color online) Left panel: LDA results for the lattice constant of $Cd_xZn_{1-x}Se$ structures as function of the Cd content. Right panel: interpolation of elastic constant values (Ref. 43), to be used in the multiband modeling.

TABLE II. Calculated stress values for model $Cd_{0.5}Zn_{0.5}Se$ structures.

| $Cd_{0.5}Zn_{0.5}Se$ | $\sigma_{xx}$ (GPa) | $\sigma_{yy}$ (GPa) | Energy (eV) |
|---|---|---|---|
| Model 1 | 2.28 | 2.28 | −28.0171 |
| Model 2 | 2.90 | 2.90 | −27.9657 |
| Average at $T=573$ K | 2.54 | 2.54 | −27.9958 |

The calculated energies of the topmost valence-band levels, with predominant $hh(0,0)$ and $lh(0,0)$ characters, are shown in Fig. 9 as a function of Cd content in the disklike-shaped dots with different height and for **B**=0. Strain effects are expected to be relevant for higher Cd contents whereas spatial confinement effects should define the electronic structure as Cd concentration $x$ decreases. Note that increasing values of $L_z$ has caused an interchange between the topmost levels with the ground state changing from hh and lh characters.

## V. DOT SIZE DYNAMICS DURING ANNEALING

As already mentioned and confirmed by HREM images, thermal annealing processes produce changes in the size and in the chemical composition of the QDs. One question is: how these competing processes are taking place and modulating the experimental optical results? There are strong evidences, as shown in Figs. 1 and 2, that the magnetic character of ground state of the *as grown* and thermally processed samples can be altered by annealing. The changes in sign in
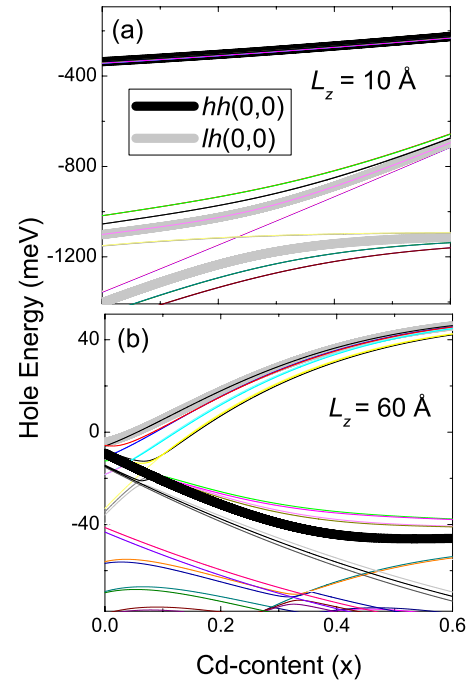


FIG. 9. (Color online) Valence-band levels with $hh(0,0)$ and $lh(0,0)$ characters as a function of the Cd content at $B=0$ T: (a) for $L_z=10$ Å and (b) $L_z=60$ Å.

the Zeeman splitting and in the magnetic field slope of both polarized emission peak positions, $[E_{\sigma(\pm)}(B) - E_{\sigma(\pm)}(0)]$, must be attributed to modification in the $p$ character of the hole ground state since the $s$ character of electron states remains nearly unchanged in the whole range of parameters considered in our analysis. It is our understanding that the evolution of the valence electronic structure is one key point which may explain these effects.

According to selection rules governing interband optical transitions, the recombination between electrons in the conduction and holes in the valence-band ground states is allowed for quantum indexes $n_+ = n_- = 0$ and $\nu = 1$ both for the heavy and light holes. According to the notation in Eqs. (3) and (10) we are labeling the character of hole states determined by the level of hybridization as hh(0,0) and lh(0,0).

Let us consider a qualitative analysis that may help the discussion about anisotropic confinement and its influence in the determination of the character of the valence-band ground state. The energy of the hh and lh carriers localized in a spatial region characterized by longitudinal, $L_z$, and lateral, $(L_x, L_y)$, dimensions are proportional to

$$E^{\text{hh}} \propto \frac{1}{m_x^{\text{hh}} \langle L_x \rangle^2} + \frac{1}{m_y^{\text{hh}} \langle L_y \rangle^2} + \frac{1}{m_z^{\text{hh}} \langle L_z \rangle^2} \qquad (20)$$

and

$$E^{\text{lh}} \propto \frac{1}{m_x^{\text{lh}} \langle L_x \rangle^2} + \frac{1}{m_y^{\text{lh}} \langle L_y \rangle^2} + \frac{1}{m_z^{\text{lh}} \langle L_z \rangle^2}. \qquad (21)$$

First consider that there is isotropy in lateral dimensions $x$, $y$ and in the lateral effective masses for each hole carrier, then we may write $m_x^{\text{hh}} = m_y^{\text{hh}} \equiv m_{xy}^{\text{hh}}$ and $m_x^{\text{lh}} = m_y^{\text{lh}} \equiv m_{xy}^{\text{lh}}$ and $\langle L_x \rangle^2 = \langle L_y \rangle^2 \equiv \langle R \rangle^2$. Therefore, the energies of the valence-band carriers are given by $E^{\text{hh}} \propto (2/m_{xy}^{\text{hh}} \langle R \rangle^2 + 1/m_z^{\text{hh}} \langle L_z \rangle^2)$ and $E^{\text{lh}} \propto (2/m_{xy}^{\text{lh}} \langle R \rangle^2 + 1/m_z^{\text{lh}} \langle L_z \rangle^2)$. We wish to find under which conditions we may observe an inversion between heavy- and light-hole ground states, or more specifically, $E^{\text{lh}} < E^{\text{hh}}$. Certainly, this inversion would require

$$\frac{2}{m_{xy}^{\text{lh}} \langle R \rangle^2} + \frac{1}{m_z^{\text{lh}} \langle L_z \rangle^2} < \frac{2}{m_{xy}^{\text{hh}} \langle R \rangle^2} + \frac{1}{m_z^{\text{hh}} \langle L_z \rangle^2}. \qquad (22)$$

According to Eqs. (13)–(15), the diagonal terms in the Luttinger Hamiltonian model show anisotropic lateral, $1/m_{xy}^{\text{hh}} = (\gamma_1 + \gamma_2)$, $1/m_{xy}^{\text{lh}} = (\gamma_1 - \gamma_2)$ and longitudinal $1/m_z^{\text{hh}} = \gamma_1 - 2\gamma_2$, $1/m_z^{\text{lh}} = (\gamma_1 + 2\gamma_2)$ hole effective-mass parameters. By replacing these values into Eq. (22), we find that lh carriers can become the ground state in the disklike-shaped dots when

$$\langle L_z \rangle < \langle R \rangle. \qquad (23)$$

This simple analysis indicates qualitatively that a tuning effect may exist between the axial and longitudinal confinements that determines when valence-band carrier level may assume the topmost position and inverting the ground-state character from the usual hh to a lh state.

We should prove that it is possible to attribute this ground-state character inversion to the modification of magnetic response, as shown in Fig. 1. Let us describe the sequence of steps followed during the QD annealing time evo-

lution that can explain the experimental observations shown in Figs. 1 and 5.

For annealing times $t_a > 10$ s, the strain effects can be strongly relaxed due to the drastic reduction in Cd content and, consequently, of the lattice mismatch at concentrations $x \simeq 0.1$. Thus, although this small strain contribution may still affect the relative carrier energy-level position, it is plausible to attribute the change in magnetic properties to effects of thermal annealing on the shape of the spatial confinement.

Our proposal for QD size dynamics explores the observed tendency of annealed dots to reach a configuration with minimum surface to volume energy ratio, as the annealing time increases. By starting with a certain value for the initial dot volume before annealing, we may assume that the QD kinematics evolves toward the equilibrium where its formation process seeks for minimal surface condition. For a cylindrical geometric shape of radius $R$ and height $L_z$, this stable configuration is attained when $\langle L_z \rangle = \langle R \rangle$. As shown in Fig. 9, an increase in the $\langle L_z \rangle$ dimension with unchanged radial size $\langle R \rangle$ leads to the interchange between the topmost valence subbands with the hh character changing to lh character.

We have used this minimum energy ratio criterion to calculate the energy levels, as a function of the magnetic field, for carriers in the conduction and in the valence bands of $\text{Cd}_x\text{Zn}_{1-x}\text{Se}/\text{ZnSe}$ QDs using Eqs. (7) and (13), respectively. These results are shown in Fig. 10. Indeed, it is possible to interchange ground-state hole character which leads to qualitative modification in the magnetic response. For increasing magnetic field the slope of the energy difference $[E_{\sigma(+)}(B) - E_{\sigma(-)}(0)]$ of the two circularly polarized emission peaks and the whole effect can be attributed to the valence-band ground-state evolution during the annealing process. Also, the inversion of the magnetic shift observed experimentally in Fig. 1 has been reproduced with success in Fig. 10(d) for the parameters that emulate the conditions previous and after annealing reported in Figs. 10(b) and 10(d).

In order to understand the evolution of the spin splitting of the ground states involved in the optical recombination we show, in Fig. 11, the calculated Zeeman splitting at $\mathbf{B} = 6$ T for the *e-h* pair transition involving one valence-band level with hh(0,0) character and another with lh(0,0) character. As the experimental data have revealed, the system suffers a drastic reduction in the Cd content during the first 10 s of annealing. Such a quick reduction is responsible for the sign reversal of the Zeeman splitting, which is associated the interchange between *spin-up* and *spin-down* hole levels in the topmost valence band with hh(0,0) character. After the 10 s, the growth in $z$ direction takes place and leads to interchange between hh and lh topmost subbands. The transition involving the new lh(0,0) ground-state character remains with the same sign of the Zeeman splitting although, as shown in Figs. 10(c) and 10(d), the energy slope with the magnetic field changes, as observed in the experiments.

For longer annealing times, where the Cd content remains almost unchanged, the experiment shows a reduction in the Zeeman splitting toward zero according to Fig. 5. The calculated Zeeman splitting involving the topmost lh subband shows this effect when associated to a slight increase in the QD radius and leaving the height, $L_z$, almost unchanged. These effects can be reproduced, as shown in Fig. 11, where
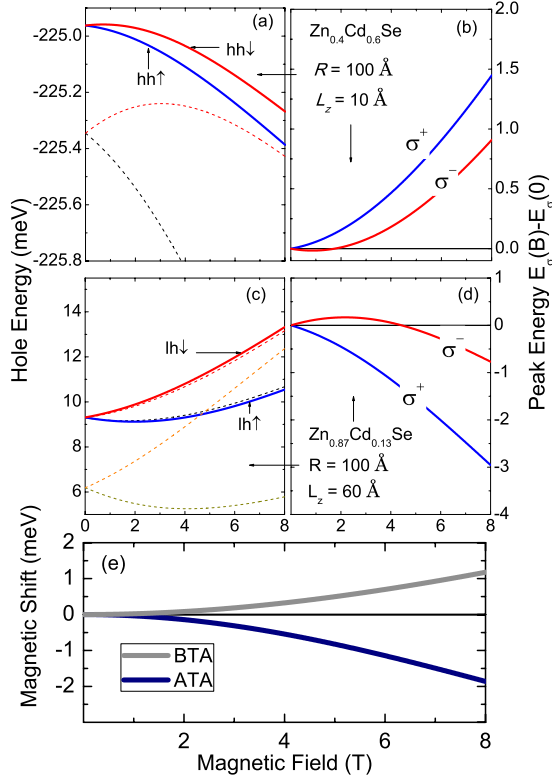
FIG. 10. (Color online) (a) Energy values of the top valence-band levels for a condition before annealing and (b) the corresponding Zeeman splitting of the *e-h* ground state. (c) Energy values of the top valence-band levels for a condition after annealing and (d) the corresponding Zeeman splitting of the *e-h* pair ground state. (e) Calculated magnetic shift from the theoretical simulation of the conditions BTA in panel (b) and ATA in panel (d).

open circles represent a plausible path for the parameters when the optical transition involves the topmost valence band with lh character.

This multiband calculation does not include any effect of Coulomb interaction on the excitonic transitions. It is however important to study the relative effect of Coulomb attrac-
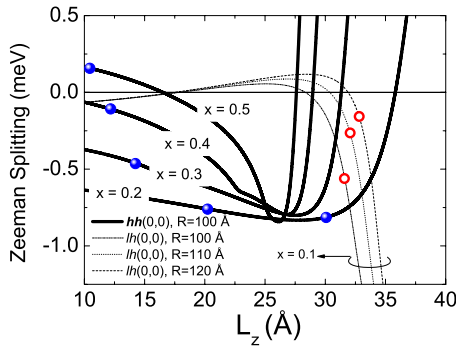


FIG. 11. (Color online) Zeeman splitting dependence, at *B* =6 T, as a function of dot height $L_z$ for different QD parameters. The Zeeman splitting is indicated for the top hh and hh levels. The symbols denote a plausible sequence of steps for the QD evolution with annealing time: filled circles when hh remains the valence-band ground state; open circles when there is the ground-state character inversion to lh.

tion and analyze the dependence of exciton binding energies on size and band-structure parameters. In order to provide some insight on the *e-h* pair formation we will assume an exciton confined in the cylindrical QD and use the parabolic approximation for both conduction and valence bands. The confinement for the pure hh and lh excitons will be described by the parabolic potential introduced above with a common value of $\omega_0$ for both electron and the hole carriers.

## VI. EXCITONIC EFFECTS

The effects of thermal annealing on the excitonic complexes has been described by using linearly polarized emission from QDs in the absence of a magnetic field.[45] Here, our approach to the *e-h* pair formation is modulated by the effective confinement produced by the applied magnetic field. Thus, it is relevant to discuss effects of electron-hole Coulomb interaction on the Zeeman splitting, linearly dependent on **B**, as well as its contribution to the magnetic shift, which shows dependence on **B** beyond the linear term. For simplicity, in this discussion, we shall take into account the limiting cases of pure hh exciton before thermal annealing and pure lh exciton after annealing. Thus, the values of the effective Landè factor for holes will be extracted from the multiband calculation.

Since the Coulomb coupling between electron and hole is attractive, one expects a blueshift of transition energies due to negative binding energies of an exciton when compared to the noninteracting *e-h* pair recombination. For a discussion of overall qualitative effects of the confinement vs Coulomb interaction we introduce the *e-h* operator $V_{e-h} = -e^2/(\kappa|\mathbf{r}_e - \mathbf{r}_h|) \equiv -e^2/(\kappa\lambda_e|\mathbf{x}_e - \beta\mathbf{x}_h|)$ that can be expanded over Bessel functions $J_p(v)$ as[46]

$$V_{e-h} = -\gamma \sum_{p=-\infty}^{\infty} e^{ip(\phi_e - \phi_h)} \int_0^\infty d\xi J_p(\xi x_e) J_p(\beta\xi x_h) e^{-\xi\alpha}.$$

(24)

In Eq. (24), $\gamma = E_{H,e}a_{H,e}/R_e$, also $E_{H,e} = e^2/(\kappa a_{H,e})$ and $a_{H,e} = \kappa\hbar^2/(m_e e^2)$ are, respectively, the effective Hartree energy and exciton Bohr radius in the semiconductor with dielectric constant $\kappa$ and electron (hole) $m_e(m_h)$ mass. The quantities $x_{e(h)} = \rho_{e(h)}/\lambda_{e(h)}$, $\beta = \lambda_h/\lambda_e$, $\xi = k\lambda_e$, and $\alpha = L_z/\lambda_e$ are introduced in order to simplify the form of Bessel function expansion. Finally, $R_{e(h)} = \sqrt{\hbar/(m_{e(h)}\omega_0)}$, $\lambda_{e(h)} = \sqrt{\hbar/(m_{e(h)}\Omega_{e(h)})}$, and $\lambda_B = \sqrt{\hbar c/(eB)}$ define effective lengths associated to the confining $(\omega_0)$, cyclotron $[\omega_{c,e(h)} = eB/(m_{e(h)}c)]$ and effective $(\Omega_{e(h)} = \sqrt{\omega_0^2 + \omega_{c,e(h)}^2/4})$ frequencies for electron and holes. Notice in this approximation, where $L_z \ll R_e$, that the perpendicular dimension enters only as a constant parameter $\alpha$ in the Coulomb interaction potential $V_{e-h}$.

It can be shown that the matrix elements $\langle \Phi_{n_e^i m_e^i \sigma_e^i} \Phi_{n_h^i m_h^i \sigma_h^i} | V_{e-h} | \Phi_{n_e^j m_e^j \sigma_e^j} \Phi_{n_h^j m_h^j \sigma_h^j} \rangle$ in the single-particle eigenfunction set $\Phi_{n,m,\sigma} = \Psi_{n_+,n_-}|\sigma\rangle$ [see Eqs. (3) and (4)] has analytical solutions in terms of Bessel function integrals when $L_z = 0$ (or $\alpha = 0$);[47] only one integral requires numerical integration for finite $L_z$. Besides, the nonzero matrix elements of $V_{e-h}$ satisfy the selection rules

$\delta_{\sigma_e^i, \sigma_e^j} \delta_{\sigma_h^i, \sigma_h^j} \delta_{m_e^i + m_h^i, m_e^j + m_h^j}$. Since we have not imposed any antisymmetrization to the two-particle wave-function product, there is no excitonic exchange Coulomb term in these matrix elements. Thus, the two-particle system spans a $n_0^2$-dimensional Hylbert space, where $n_0$ is the number of orbitals employed for the electron and hole subspaces.

In the following results we have diagonalized the total Hamiltonian which includes the exciton, $\mathcal{H}_{e-h} = \mathcal{H}_e + \mathcal{H}_h + V_{e-h}$, in the two-particle basis set $\Phi_{n,m,\sigma}$ with $n_0 = 110$ electron and hole subspaces or, equivalently, ten energy shells for each carrier. Besides the analytical solutions for the two-particle operators when $L_z = 0$, the matrix elements for one-particle operators simply become[48]

$$\langle \Phi_{n_e^i m_e^i \sigma_e^i} \Phi_{n_h^i m_h^i \sigma_h^i} | \mathcal{H}_e + \mathcal{H}_h | \Phi_{n_e^j m_e^j \sigma_e^j} \Phi_{n_h^j m_h^j \sigma_h^j} \rangle$$
$$= (E_{n_e^j m_e^j \sigma_e^j} + E_{n_h^j m_h^j \sigma_h^j}) \delta_{n_e^i m_e^i \sigma_e^i, n_e^j m_e^j \sigma_e^j} \delta_{n_h^i m_h^i \sigma_h^i, n_h^j m_h^j \sigma_h^j}, \quad (25)$$

where the eigenvalues can be expressed as

$$E_{n_{e(h)} m_{e(h)} \sigma_{e(h)}} = (2n_{e(h)} + |m_{e(h)}| + 1)\hbar\Omega_{e(h)}$$
$$+ (m_{e(h)} + \sigma_{e(h)} g_{e(h)} m_{e(h)}/2)\hbar\omega_{c,e(h)}/2$$

[see Eq. (7)], and $g_{e(h)}$ is the electron (hole) effective $g$ factor.

The band parameters for $Zn_{1-x}Cd_xSe$ QDs used in our calculation are $m_e = 0.155$ and $g_e = 0.754$, $m_h = 0.209$ and $g_h = 1.130$ (pure hh), and $m_h = 0.348$ and $g_h = -4.500$ (pure lh), with $\kappa = 8.988$. They yield effective Bohr radius $a_{H,e} \simeq 30$ Å and Hartree energy $E_{H,e} \simeq 52$ meV for electrons; similarly $a_{H,h} \simeq 23$ Å and $E_{H,h} \simeq 70$ meV for pure hh and $a_{H,h} \simeq 14$ Å and $E_{H,h} \simeq 117$ meV for pure lh. The values $a_{H,e}$ and $a_{H,h}$ determine a threshold for energy scales in the QD: when $R_{e(h)} \gg a_{H,e(h)}$ the Coulomb energy dominates whereas, for $R_{e(h)} \ll a_{H,e(h)}$, the single-particle energies are dominant. In the latter limit, the spatial carrier localization dominates ($\lambda_B \gg R_{e(h)}$) at small magnetic fields whereas, at large fields ($\lambda_B \ll R_{e(h)}$) the magnetic localization takes over and the energy spectrum collapses into Landau levels.

In order to study the competition between magnetic and spatial confinements on the excitonic spectrum, we have spanned magnetic fields **B** from 0 to 10 T, when $\lambda_B \simeq 81$ Å, and spatial parabolic confining energies, $\hbar\omega_0$, from 5 to 80 meV, which translates to parabolic spatial length for electrons, $R_e$, values changing from 100 to 25 Å, for heavy holes, $R_h$, values changing from 84 to 21 Å, and for light holes, $R_h$, ranging from 64 to 16 Å. We have also studied the effects induced by finite $L_z$ dot height, in comparison with the *flat disk* ($L_z = 0$) or pure two-dimensional QD in-plane localization.

Figures 12 and 13 show the lowest levels for hh and lh excitons in a flat-disk dot structure as a function of the perpendicular magnetic field; the plots take as reference the degenerate multiplet energy $E(B=0)$. In both figures, the lateral (vertical) QD size is increased from top to bottom (from left to right) panels; the lateral size used is the electronic value $R_e$ while the finite vertical size is always $L_z = R_e/4$. Due to the different sign of hole $g$ factors, the spin-polarized levels
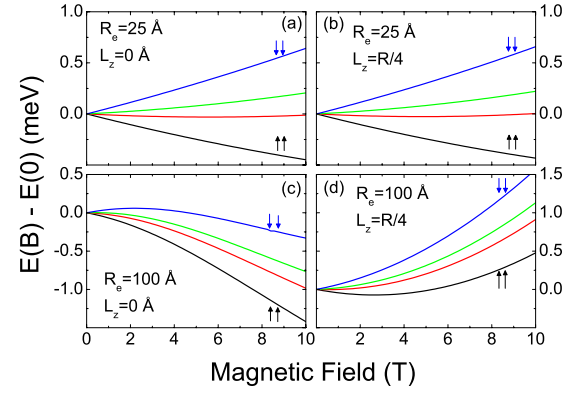


FIG. 12. (Color online) QD hh excitonic spectrum as a function of magnetic field, taken as reference the energy multiplet at $B=0$; only the lowest four levels are show, with the spin-polarized levels indicated. The respective values of lateral (electronic) and vertical QD sizes, $R_e$ and $L_z$, are shown in the panels.

are always found in the sequence indicated in the panels: for hh, ($\uparrow\uparrow$) is the first and ($\downarrow\downarrow$) is the last; for lh, ($\downarrow\downarrow$) occurs as second and ($\uparrow\uparrow$) as third levels.

The more important data to focus here are not the energy magnitudes but the relative level splitting of the spin-polarized levels, $|E(\uparrow\uparrow) - E(\downarrow\downarrow)|$, as a function of **B**. Panels (a) and (b) in Figs. 12 and 13 show that for $R_e = 25$ Å or $R_e \lesssim a_{H,e}$ regime, the Coulomb attraction has negligible effect on the lowest energy level field dispersions, as discussed above. Even for **B** = 10 T where, $R_e \ll \lambda_B$, the magnetic confinement is also negligible. Thus, for relatively small QD, the high external confining frequency ($\omega_0 \simeq 100$ meV) dictates the spectrum properties and the energy dispersions are essentially linear. In this limit, the presence of a finite perpendicular size $L_z$ does not affect the QD spectrum, as seen in panels (a) and (b). Due to the larger $|g_h|$ values, the spin splitting $|E(\uparrow\uparrow) - E(\downarrow\downarrow)|$ for lh excitons is about twice the splitting for hh.

The situation changes drastically in large size dots, or weaker spatial confinements, as can be seen in panels (c) and
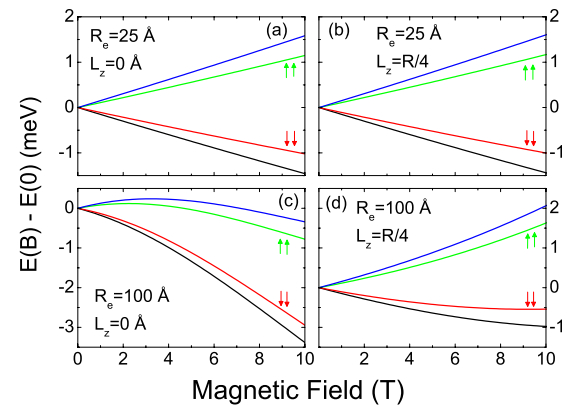


FIG. 13. (Color online) QD lh excitonic spectrum as a function of magnetic field, taken as reference $E(0)$, the energy multiplet at $B=0$; only the lowest four levels are shown, with the spin-polarized levels occurring in the indicated sequence. The respective values for the lateral (electronic) and vertical QD sizes, $R_e$ and $L_z$, are given in the panels.
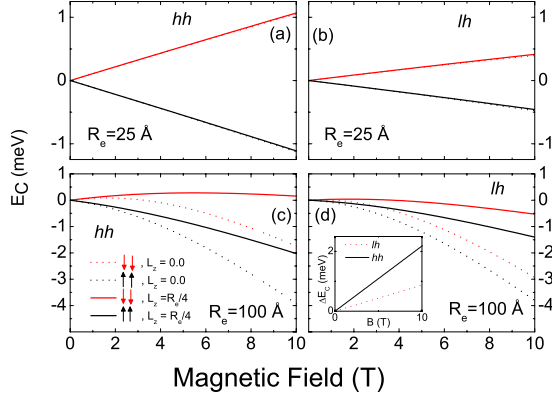
FIG. 14. (Color online) Influence of the Coulomb *e-h* interaction, $E_C$, in the total energy of the spin-polarized levels, ↑↑ and ↓↓, of all spectra shown in Figs. 12 and 13. Left (right) panels are for hh(lh), with the values of $R_e$ indicated; full (dotted) curves refer to $L_z=0(L_z=R_e/4)$, and the legend in panel (c) applies to all panels. Inset in panel (d) shows the splitting, $\Delta E_C=E_C(↓↓)-E_C(↑↑)$, of all plots in panels (a)–(d); they all fall on the same line, independent on the QD sizes, just differing for hh or lh dots.

(d) in Figs. 12 and 13, for the $R_e=100$ Å $\gg a_{H,e}$ regime. For flat-disk regime, in panel (c), the energy dispersion of all levels show downward curvature and with negative values at almost every **B**; only a slight fraction of the ↓↓(↑↑) spin-polarized energy level for hh(lh) exciton is positive in a small range of *B* values. This is the main signature where the attractive Coulomb interaction of the *e-h* pair decreases the total energy and creates strong bound excitons for increasing (decreasing) magnetic confinement (length $\lambda_B$). However, the presence of a finite $L_z$, as shown in Fig. 12(d), compensates for the hh and lh Coulomb attraction and reverses the magnetic energy dispersion curvatures as a function of **B**. These effects indicate that Coulomb interaction may play different roles for hh and lh magnetic dispersions as well as the character of a magnetic state in the dot. The inversion induced by a finite perpendicular size in large QDs indicates that the Coulomb attraction becomes week and electrons and holes can stay separated inside a QD with expanded three-dimensional-like dimensions. Also, for **B**=10 T, or $R_e>\lambda_B$, the magnetic confinement becomes important and yields the diamagnetic dispersions (upward curvatures) of the QD levels seen in panels (c) and (d).

We have seen how the Coulomb interaction plays a significant role in determining the overall features of the QD excitonic spectrum and the competing energy scales in the system. In order to explore further its influence, Fig. 14 shows the isolated contribution due to *e-h* Coulomb coupling to the total energy, where we have defined: $E_C=E-E_e-E_h$; we shall focus our attention only on the spin-polarized levels ↑↑ and ↓↓ and consider the same lateral and vertical sizes as used in Figs. 12 and 13, with the left (right) panel for hh(lh). Figure 14 shows clearly the effects discussed: at small dots (top panels), the Coulomb interaction becomes negligible and the external confinement determines the dominant energy scale. For large dots, (bottom panels) the interaction

changes drastically the linear magnetic dispersions to a diamagnetic contribution and, in this limit, a finite perpendicular size decreases the relative importance of the Coulomb attraction. This figure shows how the *e-h* attraction has different quantitative behaviors on hh and lh excitons in dots. It is interesting to note in the insets of Fig. 14(d) that the magnetic field dependence of the relative energy splitting between spin-polarized levels, $\Delta E_C=E_C(↓↓)-E_C(↑↑)$, is completely independent of the Coulomb attraction. The splitting of all curves in Figs. 14(a)–14(d) falls exactly on the same line, the only difference being the effective *g* factor for hh and lh carriers.

Hence, the *e-h* Coulomb attraction has an additional effect over the diamagnetic shift of both spin-split exciton ground states. It establishes a competition with other energy scales which depend on the QD size and magnetic field strength. However, the spin-polarized level splitting, which is one of the most relevant aspects in the magneto-optical properties discussed before, is Coulomb independent in the excitonic modeling analyzed here.

## VII. CONCLUSIONS

We have analyzed how different aspects of the experimental results for the effective Zeeman splitting in thermal annealed $Cd_xZn_{1-x}Se/ZnSe$ QDs may be experimentally characterized and theoretically simulated. We found that these effects are caused by a peculiar annealing time evolution of the band structure associated to dot changes on the chemical composition, *x*, and one shape, here described in cylindrical geometry with dimensions $R$ and $L_z$. The kinematic process during thermal annealing in $Cd_xZn_{1-x}Se/ZnSe$ QDs shows a fast interdiffusion of Cd content to the ZnSe layer and a time evolution of the quantum confinement shape. We observed that the peculiar behavior of the Zeeman splitting during thermal annealing is related to the interchange of character between the heavy- and light-hole ground states. Our analysis of this thermal annealing process and its magneto-optical properties has provided a fairly clear picture of the band-structure dependence on the system parameters and types of confinements. It has also proved that thermal annealing can be used as an effective tool to tune magnetic properties.

Finally, the ability to control microstructures based on semiconductor nanocrystals, using thermal annealing, provides opportunities for creating novel devices and can be generalized to other substrates or other synthesis techniques. Furthermore, we expect that similar effects will prove useful for other types of semiconductor alloys, including magnetic and ferroelectric materials where anisotropy effects can be further exploited.

[1] M. Bayer, G. Ortner, O. Stern, A. Kuther, A. A. Gorbunov, A. Forchel, P. Hawrylak, S. Fafard, K. Hinzer, T. L. Reinecke, S. N. Walck, J. P. Reithmaier, F. Klopf, and F. Schäfer, Phys. Rev. B **65**, 195315 (2002).

[2] R. Kotlyar, T. L. Reinecke, M. Bayer, and A. Forchel, Phys. Rev. B **63**, 085310 (2001).

[3] M. Bayer, A. Kuther, A. Forchel, A. Gorbunov, V. B. Timofeev, F. Schafer, J. P. Reithmaier, T. L. Reinecke, and S. N. Walck, Phys. Rev. Lett. **82**, 1748 (1999).

[4] T. Mensing, L. Worschech, R. Schwertberger, J. P. Reithmaier, and A. Forchel, Appl. Phys. Lett. **82**, 2799 (2003).

[5] S. Mahapatra, T. Kiessling, E. Margapoti, G. V. Astakhov, W. Ossau, L. Worschech, A. Forchel, and K. Brunner, Appl. Phys. Lett. **89**, 043102 (2006).

[6] D. Tönnies, G. Bacher, A. Forchel, A. Waag, and G. Landwehr, Appl. Phys. Lett. **64**, 766 (1994).

[7] S. Fafard and C. Ni. Allen, Appl. Phys. Lett. **75**, 2374 (1999).

[8] S. Mackowski, L. M. Smith, H. E. Jackson, W. Heiss, J. Kossut, and G. Karczewski, Appl. Phys. Lett. **83**, 254 (2003).

[9] A. I. Tartakovskii, M. N. Makhonin, I. R. Sellers, J. Cahill, A. D. Andreev, D. M. Whittaker, J.-P. R. Wells, A. M. Fox, D. J. Mowbray, M. S. Skolnick, K. M. Groom, M. J. Steer, H. Y. Liu, and M. Hopkinson, Phys. Rev. B **70**, 193303 (2004).

[10] W. Langbein, P. Borri, U. Woggon, V. Stavarache, D. Reuter, and A. D. Wieck, Phys. Rev. B **69**, 161301(R) (2004).

[11] P. E. Smith, S. H. Goss, S. T. Bradley, M. K. Hudait, Y. Lin, S. A. Ringel, and L. J. Brillson, J. Vac. Sci. Technol. B **22**, 554 (2004).

[12] R. Leon, Y. Kim, C. Jagadish, M. Gal, J. Zou, and D. J. H. Cockayne, Appl. Phys. Lett. **69**, 1888 (1996).

[13] A. Krost, J. Christen, N. Oleynik, A. Dadgar, S. Deiter, J. Bläsing, A. Krtschil, D. Forster, F. Bertram, and A. Diez, Appl. Phys. Lett. **85**, 1496 (2004).

[14] D. O. Yi, I. D. Sharp, Q. Xu, C. Y. Liao, J. W. Ager III, J. W. Beeman, Z. Liliental-Weber, K. M. Yu, D. Zakharov, E. E. Haller, and D. C. Chrzan, *Nanoscale Materials and Modeling-Relations Among Processing, Microstruture and Mechanical Properties*, MRS Symposia Proceedings No. 821 (Materials Research Society, Pittsburgh, 2004), p. 8.16.

[15] S. Mackowski, T. Gurung, H. E. Jackson, L. M. Smith, W. Heiss, J. Kossut, and G. Karczewski, Appl. Phys. Lett. **86**, 103101 (2005).

[16] E. Nabavi, T. J. Badcock, T. Nuytten, H. Y. Liu, M. Hopkinson, V. V. Moshchalkov, and M. Mowbray, J. Appl. Phys. **105**, 053512 (2009).

[17] E. Margapoti, L. Worschech, S. Mahapatra, K. Brunner, A. Forchel, F. M. Alves, V. López-Richard, G. E. Marques, and C. Bougerol, Phys. Rev. B **77**, 073308 (2008).

[18] Y. Léger, L. Besombes, L. Maingault, and H. Mariette, Phys. Rev. B **76**, 045331 (2007).

[19] H. Sanada, T. Sogawa, H. Gotoh, Y. Tokura, H. Yamaguchi, H. Nakano, and H. Kamada, Phys. Rev. B **79**, 121303(R) (2009).

[20] M. Abbarchi, T. Kuroda, T. Mano, K. Sakoda, and M. Gurioli, Phys. Rev. B **81**, 035334 (2010).

[21] C. Schulhauser, D. Haft, R. J. Warburton, K. Karrai, A. O. Go-vorov, A. V. Kalameitsev, A. Chaplik, W. Schoenfeld, J. M. Garcia, and P. M. Petroff, Phys. Rev. B **66**, 193303 (2002).

[22] J. D. Budai, C. W. White, S. P. Withrow, M. F. Chisholm, J. Zhu, and R. A. Zuhr, Nature (London) **390**, 384 (1997).

[23] W. H. Jiang, D. A. Thompson, O. Hul'ko, B. J. Robinson, and P. Mascher, J. Vac. Sci. Technol. A **24**, 700 (2006).

[24] M. Scheibner, T. A. Kennedy, L. Worschech, A. Forchel, G. Bacher, T. Slobodskyy, G. Schmidt, and L. W. Molenkamp, Phys. Rev. B **73**, 081308(R) (2006).

[25] S. J. Prado, C. Trallero-Giner, A. M. Alcalde, V. López-Richard, and G. E. Marques, Phys. Rev. B **69**, 201310(R) (2004).

[26] S. J. Prado, C. Trallero-Giner, A. M. Alcalde, V. López-Richard, and G. E. Marques, Phys. Rev. B **67**, 165306 (2003).

[27] S. J. Prado, C. Trallero-Giner, A. M. Alcalde, V. López-Richard, and G. E. Marques, Phys. Rev. B **68**, 235327 (2003).

[28] V. López-Richard, A. M. Alcalde, S. J. Prado, G. E. Marques, and C. Trallero-Giner, Appl. Phys. Lett. **87**, 231101 (2005).

[29] V. López-Richard, S. J. Prado, G. E. Marques, C. Trallero-Giner, and A. M. Alcalde, Appl. Phys. Lett. **88**, 052101 (2006).

[30] K. L. Janssens, B. Partoens, and F. M. Peeters, Phys. Rev. B **67**, 235325 (2003).

[31] V. Mlinar, M. Tadić, and F. M. Peeters, Phys. Rev. B **73**, 235336 (2006).

[32] *Numerical Data and Functional Relationships in Science and Technology*, Landolt-Börnstein Comprehensive Index, edited by O. Madelung and W. Martienssen (Springer, Berlin, 1996).

[33] G. Saint-Girons, N. Chauvin, A. Michon, G. Patriarche, G. Beaudoin, G. Bremond, C. Bru-Chevallier, and I. Sagnes, Appl. Phys. Lett. **88**, 133101 (2006).

[34] S. Fleming and A. Rohl, Z. Kristallogr. **220**, 580 (2005).

[35] W. Humphrey, A. Dalke, and K. Schulten, J. Mol. Graphics **14**, 33 (1996).

[36] GNU IMAGE MANIPULATION PROGRAM, http://www.gimp.org

[37] F. H. Pollak and M. Cardona, Phys. Rev. **172**, 816 (1968).

[38] C. Pryor, J. Kim, L. W. Wang, A. J. Williamson, and A. Zunger, J. Appl. Phys. **83**, 2548 (1998).

[39] M. Tadić, F. M. Peeters, and K. L. Janssens, Phys. Rev. B **65**, 165333 (2002).

[40] J. P. Perdew and A. Zunger, Phys. Rev. B **23**, 5048 (1981).

[41] G. Kresse and J. Furthmüller, Phys. Rev. B **54**, 11169 (1996).

[42] F. Birch, Phys. Rev. **71**, 809 (1947).

[43] I. Hamdi, M. Aouissi, A. Qteish, and N. Meskini, Phys. Rev. B **73**, 174114 (2006).

[44] S. Lankes, T. Reisinger, B. Hahn, C. Meier, M. Meier, and W. Gebhardt, J. Cryst. Growth **159**, 480 (1996).

[45] E. Margapoti, L. Worschech, A. Forchel, A. Tribu, T. Aichele, R. André, and K. Kheng, Appl. Phys. Lett. **90**, 181927 (2007).

[46] J. D. Jackson, *Classical Electrodynamics* (Wiley, New York, 1975), Chap. 3.

[47] V. Halonen, T. Chakraborty, and P. Pietiläinen, Phys. Rev. B **45**, 5980 (1992).

[48] C. F. Destefani, S. E. Ulloa, and G. E. Marques, Phys. Rev. B **69**, 125302 (2004); C. F. Destefani, S. E. Ulloa, and G. E. Marques, *ibid.* **70**, 205315 (2004).